Water Diffusion Mechanism in Carbon Nanotube and Polyamide Nanocomposite Reverse Osmosis Membranes: A Possible Percolation-Hopping Mechanism

Takumi Araki,[1,2] Rodolfo Cruz-Silva,[1,3,†] Syogo Tejima,[1,2] Josue Ortiz-Medina,[1] Aaron Morelos-Gomez,[1] Kenji Takeuchi,[1,3] Takuya Hayashi,[1,3] Mauricio Terrones,[3,4] and Morinobu Endo[1,3,*]

[1]*Global Aqua Innovation Center, Shinshu University, 4-17-1 Wakasato, Nagano 380-8553, Japan*
[2]*Research Organization for Information Science and Technology, 2-32-3, Kitashinagawa, Shinagawa-ku, Tokyo 140-0001, Japan*
[3]*Institute of Carbon Science and Technology, Shinshu University, 4-17-1 Wakasato, Nagano 380-8553, Japan*
[4]*Department of Physics, Chemistry, Materials Science and Engineering, Center for 2-Dimensional and Layered Materials and Center for Atomically Thin Multifunctional Materials (ATOMIC), The Pennsylvania State University, University Park, Pennsylvania 16802, USA*

(Received 12 July 2017; revised manuscript received 12 September 2017; published 20 February 2018)

This paper is a contribution to the Physical Review Applied *collection in memory of Mildred S. Dresselhaus.*

The mechanism of water diffusion across reverse osmosis nanocomposite membranes made of carbon nanotubes (CNTs) and aromatic polyamide is not completely understood despite its high potential for desalination applications. While most of the groups have proposed that superflow inside the CNT might positively impact the water flow across membranes, here we show theoretical evidence that this is not likely the case in composite membranes because CNTs are usually oriented parallel to the membrane surface, not to mention that sometimes the nanotube cores are occluded. Instead, we propose an oriented diffusion mechanism that explains the high water permeation by decreasing the diffusion path of water molecules across the membranes, even in the presence of CNTs that behave as impermeable objects. Finally, we provide a comprehensive description of the molecular dynamics occurring in water desalination membranes by considering the bond polarizability caused by dynamic charge transfer and explore the use of molecular-dynamics-derived stochastic diffusion simulations. The proposed water diffusion mechanism offers an alternative and most likely explanation for the high permeation phenomena observed in CNTs and PA nanocomposite membranes, and its understanding can be helpful to design the next generation of reverse osmosis desalination membranes.

DOI: 10.1103/PhysRevApplied.9.024018

I. INTRODUCTION

Highly cross-linked aromatic polyamide (PA) is a polymer widely used as the active layer in seawater desalination membranes due to its easy synthesis and excellent salt rejection rate of up to 99.8% [1]. This polymer results from the interfacial polymerization of 1,3,5-benzenetricarbonyl trichloride (TMC) with *m*-phenylenediamine (MPD). It is typically prepared by soaking a highly permeable porous support membrane in an aqueous solution of MPD, followed by immersion of this porous membrane in an organic solution of TMC, where a 100- to 200-nm-thick aromatic polyamide film is quickly formed on the surface of the support membrane. The effect of several parameters and additives on the preparation of this type of membrane has been studied for many years [2]. One of the major innovations in this field was the preparation of nanocomposite PA films. Among the most studied nanomaterials are zeolites [3,4], titanium oxide [5,6], silica nanoparticles [7], graphene oxides [8–10], and carbon nanotubes [11–16]. These nanocomposite membranes of PA often show increased salt rejection and water transport; however, the detailed mechanism of water diffusion has barely been studied, and it is still a topic of discussion. For zeolite-polyamide systems, several hypotheses have explained the enhanced flux. Some of them are higher water flow through the nanoparticles [17] and/or within the nanoparticle-polyamide interface. Carbon materials offer a wide range of building blocks that can be used for desalination and separation membranes [18,19]. Among the different nanocarbon types, carbon nanotubes (CNTs) offer enormous potential for synthesizing enhanced reversed osmosis (RO) membranes. CNTs can be produced in large quantities [20] and have been widely studied for many

*Corresponding author.
endo@endomoribu.shinshu-u.ac.jp
†Corresponding author.
rcruzsilva@shinshu-u.ac.jp

applications [21,22] due to their unique physical and chemical properties [23]. In the case of the CNTs and PA nanocomposites, several works have experimentally demonstrated that the addition of these one-dimensional nanomaterials can improve both water flow and salt rejection. We recently published a study of the hydration of model membranes made of single-walled CNT PA and compared it with plain PA membranes [24]. One of the most interesting results found in that work was that CNTs can induce a specific topology on the PA structure during polymerization, thus, constraining the PA mobility and avoiding the formation of water pockets during hydration. The formation of these pockets can help solvated ions to diffuse across the membrane. Despite the many studies reporting improved flux and/or rejection rate of salt from nanocomposite CNT and PA membranes [8,11–16,25–29], the mechanism of the ion and water diffusion is not well understood. Some authors have proposed that water flowing inside the hollow core of carbon nanotubes is a significant factor for the overall permeation increase [11,14,27]. Indeed, theoretical [30] and experimental results have shown that very high water flow rates within the hollow core of carbon nanotubes are possible, and it is an advantageous property for the development of membranes with vertically oriented CNTs. However, this hypothesis is not likely the case of many synthesized CNT and PA membranes, where most of the carbon nanotubes are usually oriented parallel to the membrane surface, and in the case of multiwalled CNTs, the core exhibits closed compartments that prevent the flow of water molecules through the nanotubes. Achieving composite membranes with vertically aligned CNTs is also very challenging. For interfacially synthesized membranes, CNTs act as Pickering stabilizers at the water-organic interface, and, consequently, they self-align parallel to the interface to minimize their conformational energy. Similarly, for nanotubes that are simply deposited or adsorbed onto the support membrane surface, lying flat on the surface is the minimized conformation energy. Indeed, our experimental results [13] show that CNTs are mainly oriented parallel to the membrane surface, and most of the time, they are embedded within the PA matrix. These facts are usually not considered when explaining the high permeation of CNT nanocomposite membranes. In this work, we propose a mechanism explaining the water flow across nanocomposite membranes in which the nanotubes create low-free-energy wells that guide the diffusion of the water molecules across the membrane, thus, resulting in shorter trajectories and improving the water permeation across the membrane through a mechanism of oriented percolation diffusion. We hope the present model can contribute to the design of better nanocomposite reverse osmosis membrane systems with high performance which are highly required in the 21st century.

II. EXPERIMENTAL PART

A. Simulation method

Classical molecular-dynamics simulations are performed by the LAMMPS simulation package [31]. The overall procedure used to build the PA model structure is similar to our previous work [24]. Briefly, TMC molecules are used as seeds for constructing the plain PA structure where TMC molecules are adsorbed on a CNT surface. An *in silico* polymerization is carried out by step growth of the structure following a set of rules that considers the possible formation of the cross-linked matrix, as well as topological features such as four and six membered rings and carboxylic groups. For the plain PA model, we start with ten TMC molecules as seeds within a virtual cell of $71.8 \times 51.4 \times 65.0$ Å, where 360 and 282 MPD and TMC molecules are added, respectively. For the CNT and PA model, the cell size is the same, and ten MPD molecules are first adsorbed on a CNT surface. In this case, 291 and 228 MPD and TMC molecules are added, respectively. The CNT exhibits a triple-walled armchair structure [(15,15), (10,10), and (5,5)] with a total of 2520 carbon atoms. After polymerization, a geometrically optimized structure is obtained by running a 200-ps (0.5-fs step) molecular dynamics under the *N*-*P*-*T* ensemble, keeping the pressure at 1 atm and room temperature to minimize the energy of the structure.

For classical molecular dynamics, the extended single point charge (SPC/E) model [32] is adopted for water molecules. We use the general Assisted Model Building with Energy Refinement (AMBER) force field (GAFF) [33] for the intermolecular interaction force calculations in both the plain PA and the CNT and PA composite. The GAFF force field has given good results to describe fully aromatic polyamides [34–36]. The partial charges of PA are calculated using ANTECHAMBER 1.27 and AM1-BCC [37,38]. The interactions between molecules are calculated by Lenard-Jones potentials using the Lorentz-Berthelot mixing rules, while the Coulombic interactions are computed with the particle-particle mesh solver [39] to a precision of 10^{-6}. All MD simulation time steps are set to 1 fs, and trajectory data are recorded every 10 000 steps for analysis. All calculations are carried out under periodic boundary conditions.

B. Charge-transfer calculations for the membrane model

We consider the charge transfer from the PA structure to the graphene layer by using the charge equilibration method (QEq) [40,41]. The QEq method minimizes the electrostatic energy of the membrane by adjusting the partial charge on individual atoms based on interactions with their neighboring atoms under an *N*-*P*-*T* ensemble. We estimate the charge values to one still frame of the membrane models using the QEq method. We use these values to adjust the charge of the atoms for the MD simulation during 100 ps while using

the GAFF, which considers the electrostatic repulsion between charges. We repeat this procedure for 500 ps and obtain an energy-minimized model that considers charge transfer. Charge-difference calculations are performed using density-functional theory as implemented in QUANTUM ESPRESSO [42] employing a plane-wave basis set and pseudopotentials. Specifically, ultrasoft pseudopotentials are employed for carbon, nitrogen, oxygen, and hydrogen. These potentials consider a Perdew-Burke-Ernzerhof model [43] for the exchange-correlation terms. For relaxation calculations, the cutoff energy is set to 35 Ry for the wave functions and van der Waals (VDW) forces are considered. The nominal charge of the atoms is set by using first-principles calculations of a relatively small oligomer in vacuum. The charge-difference two-dimensional (2D) maps are calculated by subtracting the original charges from the model accounting for change transfer. During the calculations of charge density and water density, we approximate the atom size as a Gaussian distribution with σ centered at the VDW radius of the GAFF and SPC/E models. The density values are calculated as follows:

$$\rho(x_i, y_j) = \sum_{k=1}^{N} \frac{q_k}{\sqrt{2\pi\sigma_k}} \exp\left[-\frac{(x_i, x_k)^2 + (y_i, y_k)^2}{2\sigma_k^2}\right], \quad (1)$$

where N is the number of atoms, and k represents atom index. σ_k is the VDW radius for each atom type. For charge-density plotting, q_k equals the charge values of each atom obtained by the QEq method. For the water-density plotting, q_k is set to 1. The water diffusion is calculated by averaging the individual diffusion coefficients D_i calculated for each water molecule with the following equation:

$$D_i = \lim_{t\to\infty} \frac{|r_i(t) - r_i(0)|^2}{6t}, \quad (2)$$

where $r_i(0)$ is the initial spatial coordinate, and $r_i(t)$ is the spatial coordinate at time t. The membrane region is analyzed by dividing it into a small mesh (size of 0.5×0.5 Å), and the average diffusion coefficient of the oxygen of water molecules and its density is computed for building the maps.

Hydration, desalination simulations, and ion-transport calculations are carried out by locating the membrane within an aqueous environment. The number of water molecules is 13 645 and 13 295 in the CNT and PA and plain PA models, respectively. MDs simulations are run for 10 ns using the N-P-T ensemble at 1 atm. For the hydration and ion-transport calculations, water molecules and ions are located on both sides of the membrane. For the desalination simulation, MD simulations of seawater permeation are performed using the graphene piston method. We locate a seawater (3 wt % NaCl solution, 5000 H_2O molecules, and 47 NaCl molecules) reservoir on one side of the membrane and pure water at 1 atm on the opposite side. Subsequently, the reverse osmosis process is performed using a graphene wall as a piston to apply pressure (5 MPa) on the seawater reservoir. The PA membrane is kept in its position by fixing ten carbon atoms on its initial position by using a simple spring potential ($k = 50.0$ kcal/mol Å^2). The magnitude of the spring constant is low enough to avoid inducing stiffness to the molecular network. After 10 ns of simulation, the membrane reaches a steady state of hydration, and we analyze the following 20 ns of data. In order to quantify the permeated molecules, boundaries for the top and bottom of the membranes are set at fixed values in a similar fashion as Kolev and Freger [44].

C. Selection of the CNT and PA model

In our previous work [24], we used multi-walled CNTs with (10–12)-nm diameters of more than five carbon layers to prepare CNT and PA nanocomposite RO membranes. In such large-diameter CNTs, the chirality of the concentric shells might vary from one to another, thus, playing a minor role compared to the charge transfer between the CNT outer layers and the PA structure. Thus, we use a triple-walled CNT which can be used as a model for charge transfer of the few outer layers of the multi-walled CNTs. We also

TABLE I. Different charge-transfer magnitudes as a function of CNT types.

	No. 1	No. 2	No. 3	No. 4	No. 5
Tube type	Triple-walled CNT	Triple-walled CNT	Triple-walled CNT	Single-walled CNT	Single-walled CNT
Morphology	Reference structure[a]	Shorter length	Shorter length, larger diameter	Metal	Semiconductor
CNTs chirality	(15, 15) (10, 10) (5, 5)	(15, 15) (10, 10) (5, 5)	(25, 25) (20, 20) (15, 15)	(15, 15)	(24, 2)
CNT length	5 nm	3 nm	3 nm	5 nm	5 nm
CNT diameter	2.1 nm	2.1 nm	Approximately 3.4 nm	2.1 nm	2.0 nm
Atom number	2520	1560	3120	1260	1256
CNT and PA contact area	33.0 nm^2	19.8 nm^2	32.0 nm^2	33.0 nm^2	31.4 nm^2
Charge-transfer value	−3.18 e	−1.81 e	−3.41 e	−1.82 e	−1.79 e

[a]Description of the following nanotubes is compared to tube no. 1 as reference structure.

study the charge transfer of other types of CNT structures, and the results are shown in Table I.

Single-walled CNTs are very interesting, but they do not show charge-transfer phenomena between concentric shells, and we find that compared to triple-walled CNTs (nos. 1–3), the charge-transfer magnitude decreases according to the number of atoms, regardless of being conductive (no. 4) or semiconductive (no. 5). We rule out the double-walled nanotubes to avoid a polarized structure with a negatively charged outer layer and a positively charge inner layer. In the case of the triple-walled CNTs, we find that the charge-transfer magnitude depends mainly on the CNT and PA contact area and CNT atom number. Indeed, with a shorter-length CNT (no. 2), the magnitude of the charge transfer diminishes accordingly, and a CNT with a short length and similar contact area (no. 3) shows a similar charge-transfer effect.

D. Monte Carlo simulation

Since the dimensions of the MD box are small compared to a real membrane, we carry out a simplified Monte Carlo study to simulate water permeation across a 200-nm-thick nanocomposite membrane using a random-walk method [45] that considers the molecular diffusion and free-energy data derived from MD simulations. This type of multiscale simulation has been used before to calculate the absorption properties of mesoporous materials [46,47]. The algorithm and velocity profiles are shown in the Supplemental Material [48]. Briefly, a 2D simulation cell is built, and a fixed amount of CNTs oriented parallel to the membrane surface are randomly located inside the box. Subsequently, we calculate the free-energy-potential field of the cell. For the plain PA, the free energy of the cell has a constant value, whereas the CNT and PA membrane forbids the molecule to diffuse within the CNTs and uses an inhomogeneous field calculated from the MD simulations. We place water molecules on one side of the membrane and let them move randomly according to a velocity distribution calculated from MD. During each step, the kinetic energy of water is compared to the free energy of a new position calculated randomly from the distribution of water velocities, and the movement is restricted only if the potential field of the new position is higher than the current kinetic energy. This step is repeated until the water molecule reaches the membrane bottom and the total time is computed. The permeation time is considered as the total time for the molecule to go from $z = 200$ to $z = 0$ in the simulation cell. Since random-walk times have a wide distribution, we simulate 1000 paths in order to have a representative trend.

III. RESULTS AND DISCUSSION

A. Membrane model structures

The reliability of polymer MD depends largely on an accurate description of the polymer structure. Therefore, we compare our models with other simulation models describing atomic compositions and degree of cross-linking. Table II shows the atomic composition of our membranes built when compared with other structures used in studies by Harder *et al.* [34] and Kolev and Freger [44]; they show good agreement, particularly with the latter comparison. The latter also compared the atomic composition with experimental results obtained by Rutherford backscattering spectroscopy [49]; thus, we can claim good agreement between our model and the experimental data. A distinctive feature of our CNT and PA membrane model is that it contains a CNT embedded in the PA matrix, the surrounding immediate aromatic moieties of PA are oriented parallel to the CNT surface, and they strongly interact with the CNT by VDW forces, as it has been observed experimentally [13,24].

TABLE II. The atomic composition concentration of PA (excluding hydrogen). The cross-linking degree is defined as $N/(N + COOH) \times 100\%$, and the carboxyl ratio is the COOH/C ratio.

	Previous work		This work	
Species	Harder *et al.* [34]	Kolev and Freger [44]	PA	CNT and PA
C at. %	68.7	74.4	73.8	73.9
O at. %	17.8	13.5	12.5	12.3
N at. %	9.3	12.1	12.1	12.4
Carboxyl ratio	4.2	0.8	1.6	1.4
Cross-linking degree	68.8	93.4	88.3	89.5

B. Charge transfer in the polyamide and CNT composite

When comparing our current data with our previous work [24], we have improved the CNT and PA membrane description level by considering charge-transfer effects between the polymer and the CNT. We use the QEq method that considers the geometry, ionization potentials, atomic radii, and electronic affinity to continuously calculate the atomic charges of the atoms during MD simulations. Since the large membrane model is too big to calculate the charges by *ab initio*, we use an aromatic polyamide oligomer and graphene system as a control to compare the *ab initio* calculations with the QEq results [48]. These results show relatively good agreement using considerably lower computational resources [40]. The magnitude of the charge transfer calculated by QEq can be visualized by plotting the difference with the original charges. Figure 1(a) shows the cell of the CNT and PA in a relaxed state. We calculate the charge transfer of this structure using the QEq method and subtract the original charge given by the CNT and PA model. Figure 1(b) shows the charge-transfer density plot for the CNT after relaxing the structure. The electron transfer from the PA to the CNT results in a total negative charge of $-3.18\ e$ for the entire

membrane (for a 5-nm-length CNT and PA section) or that is mainly accumulated on the outer tube (−2.25 e); however, the middle tube and inner tube have −0.48 and −0.45 e, respectively. Because of the charge-neutrality effect, the PA matrix charge increases to a positive charge of +3.18 e. Most of the electron transfer occurs from the hydrogen and carbon atoms of the aromatic rings of PA to the CNT, with an electron-transfer contribution of 48% and 33%, respectively. The rest of the charge transfer is provided by the nitrogen and oxygen atoms of the amide groups contributing to the electron transfer by 12% and 7%, respectively. The relative contribution of charge transfer from the aromatic rings and the amide moieties is plotted in Figs. 1(c) and 1(d), respectively. As expected, the charge transfer is stronger on the first layer of oriented aromatic rings lying directly on the surface of the CNT. In our previous publication [24], we found that aromatic monomer adsorbs on the surface of the CNT and remains attached to it during the polymerization due to strong van der Waals forces. Here, we find that these strongly adsorbed rings result in a charge-transfer complex formation due to the strong electrostatic attraction occurring between the negatively charged CNT and the positively charged PA. This complex interacts with the water molecules during the hydration, thus, affecting the ion-transport and diffusion mechanism.

C. Membrane hydration

Aromatic PA prepared by the reaction of TMC and MPD is a highly cross-linked structure, in which detailed structural characterization is challenging due to the lack of crystalline areas. For this reason, we use parameters such as density, radial distribution functions, and diffusion in order to study the effect of the CNT addition. For the density, we first subtract the PA membrane voids using the

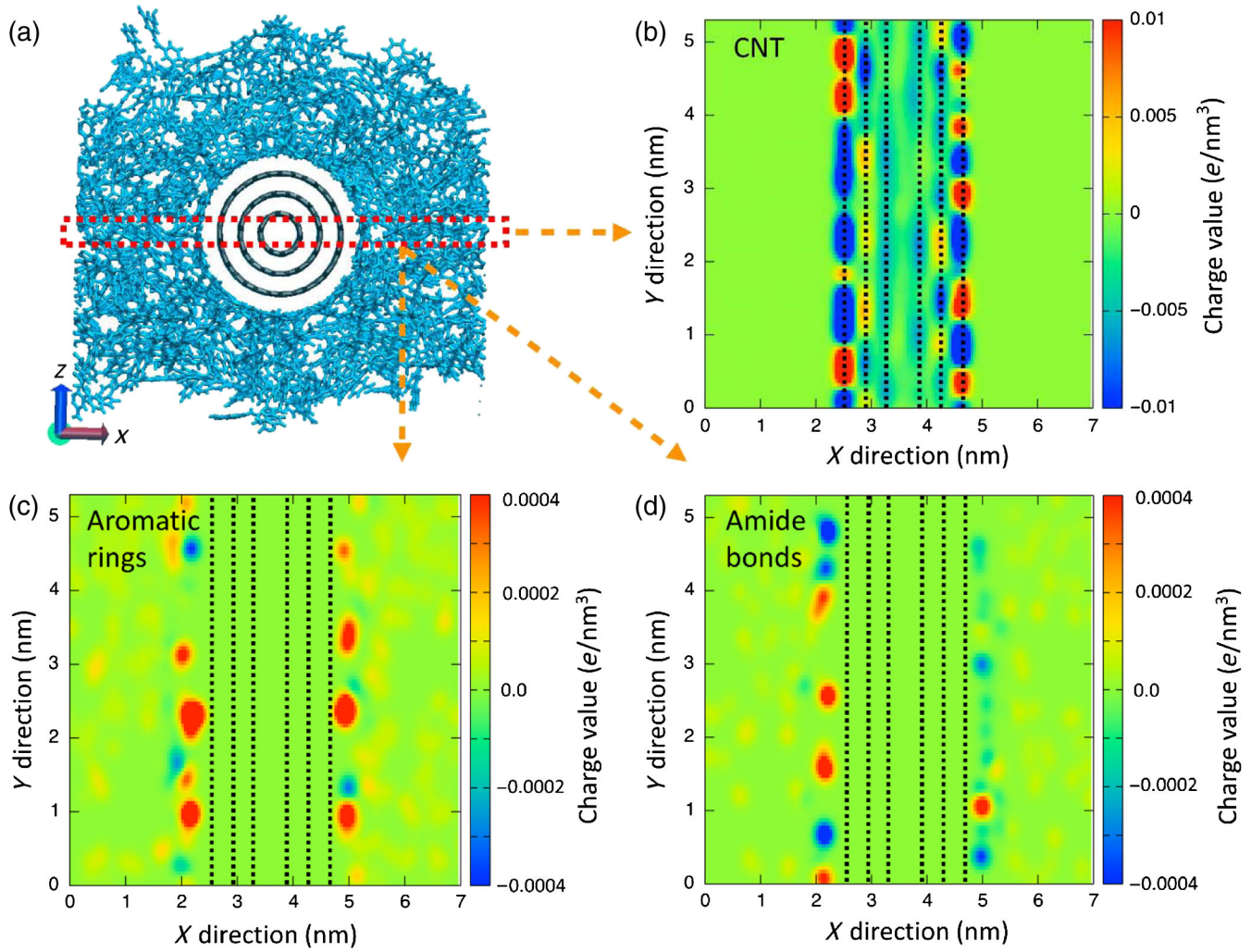

FIG. 1. Charge-transfer maps between the CNT and the PA in the composite membrane model. (a) The CNT and PA model structure after relaxation. The section within the dotted red line box is analyzed for charge transfer. Charge-transfer analysis of (b) the CNT structure, (c) the aromatic rings of the PA, and (d) the amide bonds of the PA. Negatively charged areas (electron rich) are represented in blue, while positively charged areas are represented in red.

FPOCKET code [50], and for the CNT and PA model, we exclude the CNT region for this calculation. The density of PA in the CNT and PA nanocomposite changes from 1.35 g/cm^3 in a dry state to 1.32 g/cm^3 (−2.2%) after hydration. This small yet reproducible change is similar to our previous paper [24], and apparently, it is not affected by the charge transfer. In addition, the density of the plain PA changes from 1.36 to 1.29 g/cm^3 (−4.3%) before and after hydration. The magnitude of this change is consistent with the experimental values found for a commercial membrane (FT-30) that exhibits the same chemical structure [51]. The effect of the CNT on the topology of the PA is clear from the amide bond density plot as a function of the CNT surface distance The formation of a charged-transfer complex between the PA and the CNT increases the density of the amide bonds near the surface of the CNT [see Fig. 2(a)] when compared to that of the pure PA [Fig. 2(b)]. The plot shows a series of concentric layers with different density, specifically, the region from 0.2 to 0.58 nm is the first layer, the region from 0.58 to 0.85 nm is the second layer, and region above 0.85 nm is a third diffuse layer. These concentric shells can also be seen clearly in Fig. 2(c), where we plot the amide bonds and water density as a function of the distance to the CNT surface. The effect of the matrix ordering in the proximity of the nanotube is reflected by the density fluctuations shown by the water-density plot, and the correlation between them suggests a strong effect of the polyamide topology on the water distribution of the hydrated membrane. This topology in turn, results from the CNT and PA strong interactions. After the first high-density shell, there are second and third layers of polyamide that are less dense and far from the CNT, the last one being basically indistinguishable from the bulk PA matrix. Figure 2(d) depicts the radial distribution function of the

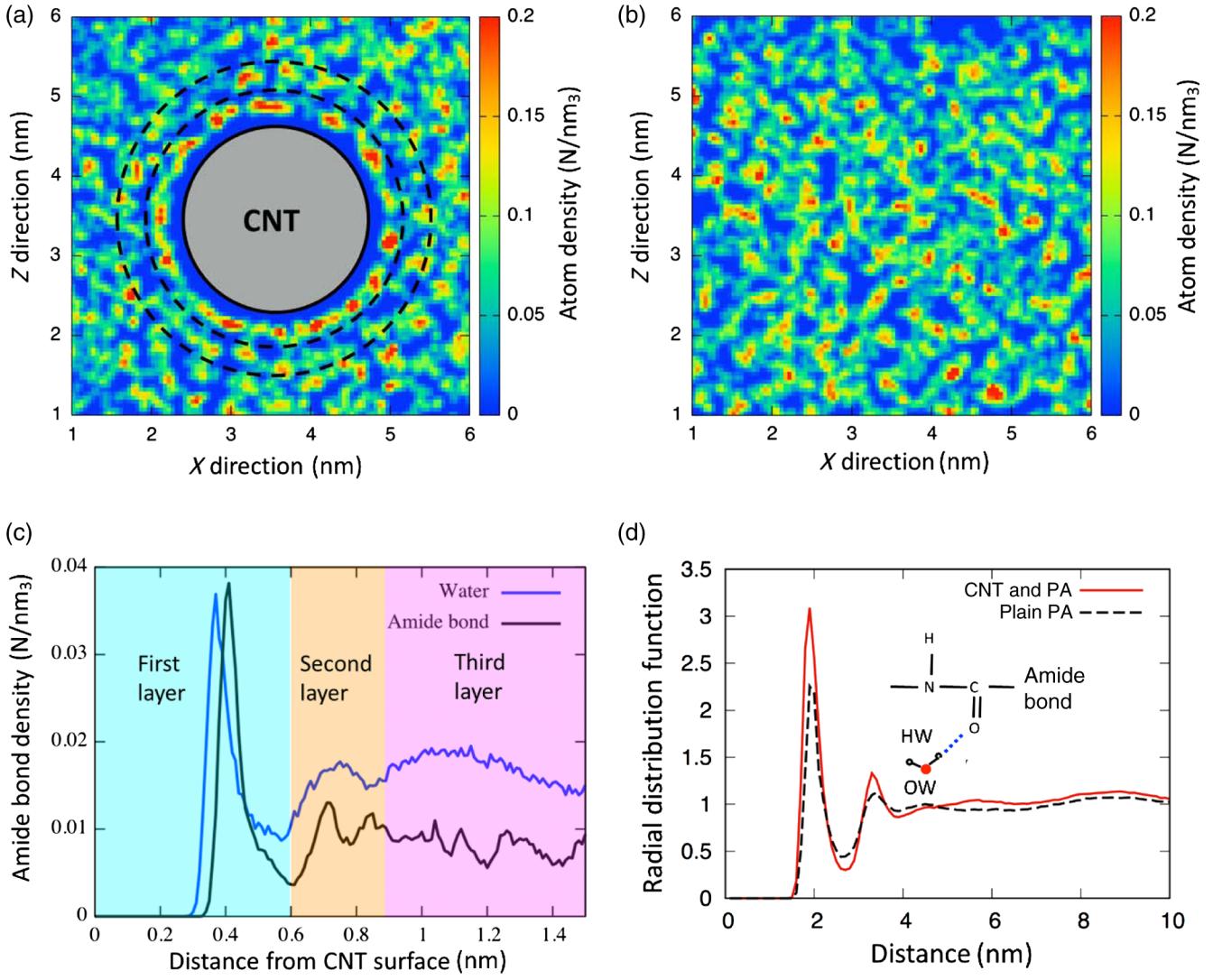

FIG. 2. Amide bond density maps of (a) the hydrated CNT and PA model membrane and (b) the hydrated plain PA membrane. Notice the high-density shell of amide bonds on the surface of the CNT. (c) Water and amide bond spatial density plotted as a function of the distance to the CNT surface. (d) Radial distribution functions between the amide bonds and the water molecules.

strongest interaction between PA and water molecules in the hydrated models. The amide bond is usually polarized and interacts with water by dipole forces ($>C^{\delta+} = O^{\delta-} * * * H{-}O{-}H$), the increment of the first and second neighbor peak intensity that indicates a better packing of the water molecules with the PA in the CNT and PA membrane. The radial distribution function (RDF) results for the plain PA membrane show good agreement with those reported in the literature [52].

After analyzing the spatial distribution of water by the RDF analysis, we also study its diffusion and distribution by using density and velocity maps. Figure 3(a) shows that the CNT and PA membrane (between 2 and 5 nm in the z axis) has a higher water density compared to the plain PA shown in Fig. 3(b). Indeed, the average water mass percentages after full hydration are 23 and 19 wt % for the CNT and PA and plain PA membranes, respectively. These results apparently disagree with density changes during hydration; however, it is explained with the volume change of the membrane upon hydration due to PA-water attraction and repulsion forces. For the more hydrophobic membranes, such as the pure PA, during hydration there is a larger expansion caused by repulsive forces which results in a higher decrease of density (−4.3% for the pure PA vs −2.2% for PA and CNT) despite absorbing less water (19 vs 23 wt %) than the PA and CNT membrane. The average water density in the CNT and PA membrane is 0.15 N/nm^3, while for the plain PA, it is 0.12 N/nm^3. This difference is most likely caused by the amide bond structure shown in Fig. 2(a), as well as the differences observed in chain mobility after hydration. The average diffusion coefficients of water molecules within the membranes are 0.45×10^{-5} and 0.31×10^{-5} cm^2/s for the nanocomposite CNT and PA and the plain PA membranes, respectively. The higher diffusion of water in this model contrasts with our previous paper [24], so it is highly likely that the hydrophilicity originated from the charge transfer improves water diffusion. The diffusion coefficient value of the plain PA membrane is in close agreement with that reported in other MD simulations [34–36,44], which is rather independent of the water model used, i.e., TIP3P, TIP4P/2005, etc. The diffusion coefficients for both the CNT and PA

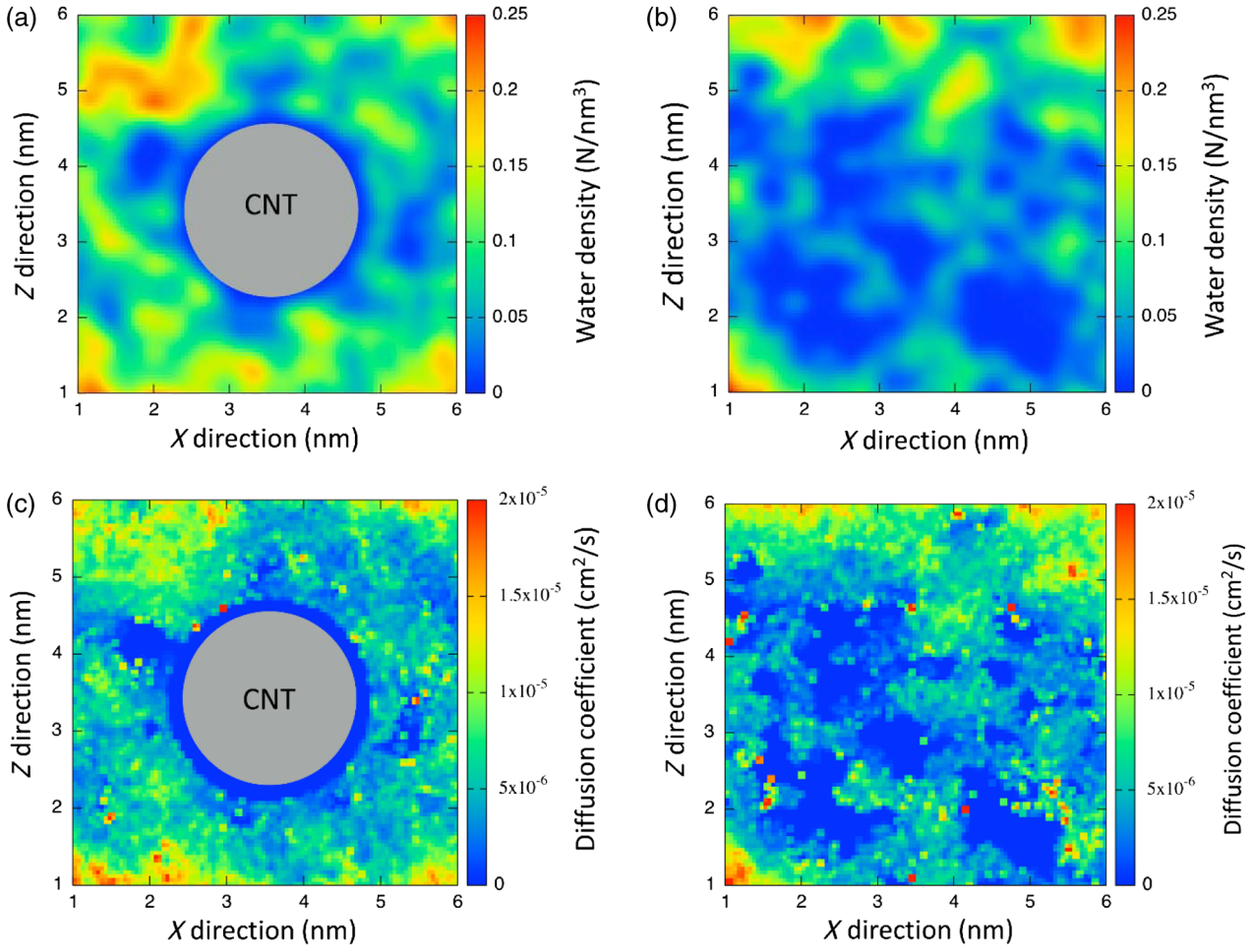

FIG. 3. Water-density maps comparing the hydrated states of (a) the CNT and PA model membrane and (b) the plain PA membrane. Plots showing the individual diffusion coefficient of water molecules in (c) the CNT and PA model membrane and (d) the plain PA membrane. Notice the formation of water-free regions of the plain PA after hydration.

and plain PA are within the typical range observed in other MD publications, which goes from 0.14×10^{-5} to 0.51×10^{-5} cm^2/s [34,35]. We also map the individual diffusion coefficients of water molecules sampled at each 10 ps in order to look for inhomogeneities on the structure after hydration on both the PA and CNT [Fig. 3(c)] and plain PA [Fig. 3(d)].

The pure PA map shows a high amide bond density region formed in these membranes that have very low water molecule density or even the absence of water. These heterogeneities arise from a phase separation observed at the nanoscale that occurs during water hydration, and it is possible due to the large PA matrix mobility, but it is effectively prevented for the CNT-reinforced PA membrane [53]. From these results, we conclude that the presence of CNT hinders the phase separation of the membrane due to the strong interactions by VDW forces with the first layer of aromatic moieties of the PA matrix, which, in turn, propagates into the bulk effectively due to the highly cross-linked structure, thus, reducing the chain mobility of the composite.

D. Ion-transport and desalination permeation studies

Figures 4(a) and 4(b) show the density profile distribution of water across the CNT and PA and plain PA membranes, respectively. The gray color area ($0.3 < Z < 5.7$ nm) in all plots corresponds to the membrane section, and in the composite membrane [Figs. 4(a) and 4(c)], the CNT area ($2.2 < Z < 4.4$ nm) is indicated in orange in the figure. The peak-shaped profiles are due to variations in the membrane local density, and it is consistent with other reports [54]. Figures 4(c) and 4(d) are the Z-averaged density profile data for Na^+ and Cl^- ions. In these plots, the ion density profiles show apparently unusual local high-density regions indicated by the spikes in Figs. 4(c) (CNT and PA) and 4(d) (plain PA). These peaks do not correspond to noise, but a trajectory analysis shows that Na^+ and Cl^- ions are trapped by polarized amide bonds of the PA [55]. When compared to the CNT and PA membrane [Fig. 4(c)], the plain PA membrane [Fig. 4(d)] exhibits a higher number of trapped Na^+ and Cl^- ions. This is mainly due to the lower chain mobility of the PA phase of the nanocomposite

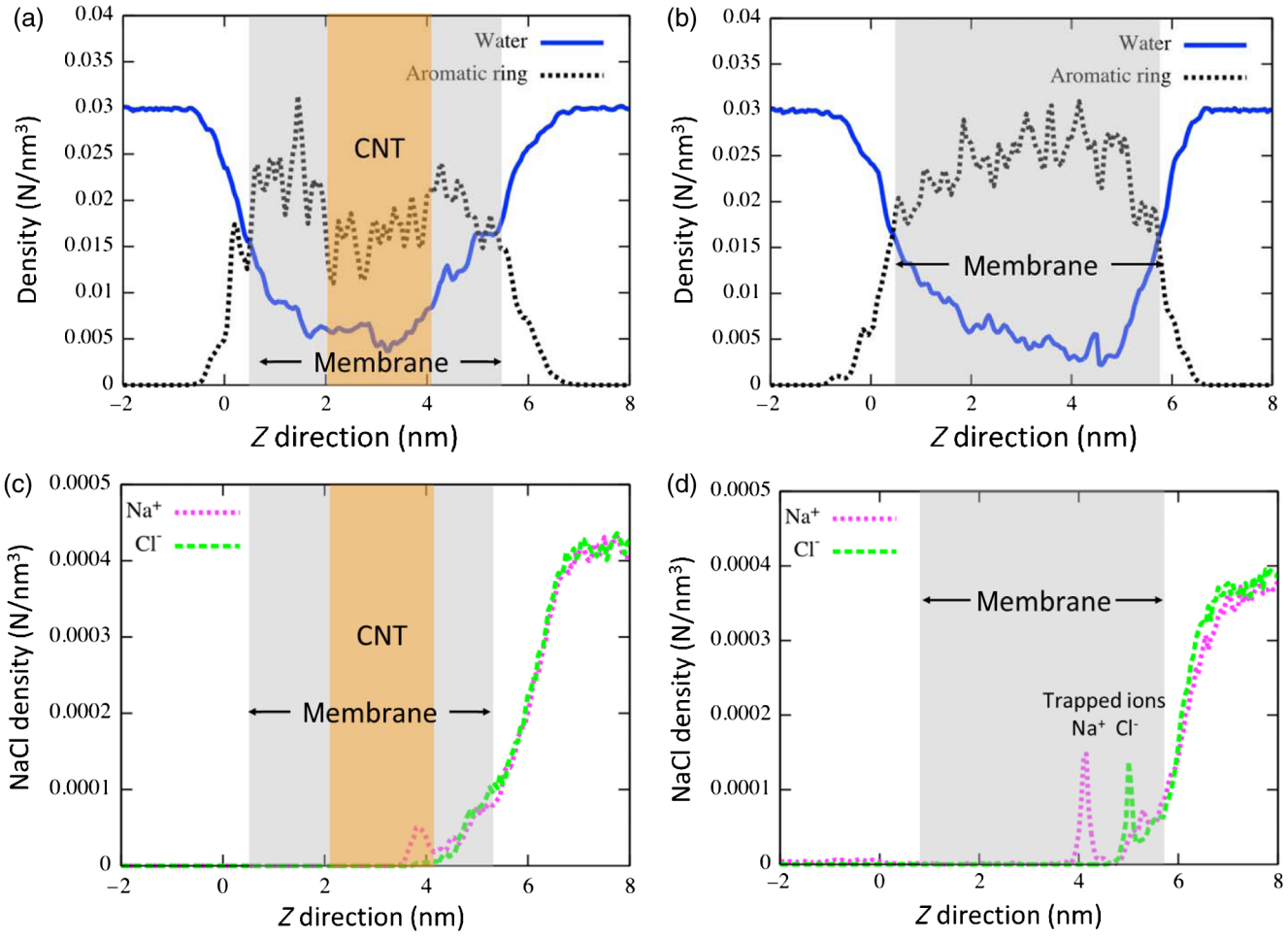

FIG. 4. Spatial density profiles of water (blue line) and aromatic rings (black line) across the (a) nanocomposite CNT and PA membrane and (b) plain PA membrane. Membrane boundaries are defined as the intersection points of water and aromatic ring density. Spatial density profiles of Na^+ and Cl^- ions in (c) the nanocomposite CNT and PA membrane and (d) the plain PA membrane.

membrane that avoids the formation of larger pores that allow the entrance or trapping of solvated ions [24].

We study the effect of the charge transfer between the PA and the CNT on the ion mobility during a simulated permeation using the piston method. Figure 5(a) shows the setup used to hydrate the membranes within two reservoirs, one with seawater on top and pure water at the bottom. We analyze the Gibbs free energy (ΔG) of ions and water permeation by Z-density profile data of Na^+, Cl^-, and water by using the following equation [56]:

$$\Delta G_i(z) = -k_B T \log[\rho(z)/\bar{\rho}], \tag{3}$$

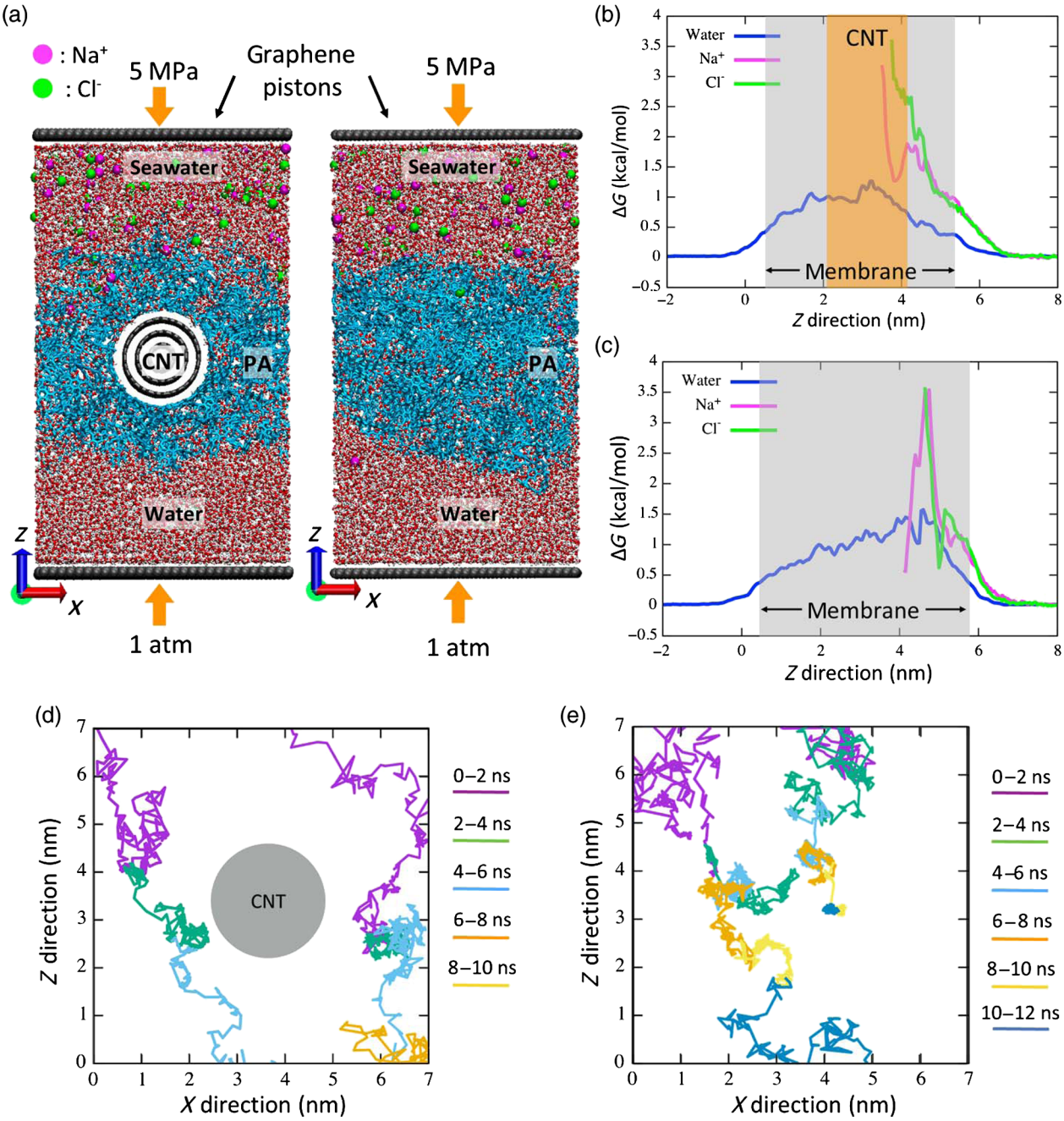

FIG. 5. (a) Molecular-dynamics setup for the desalination using the piston simulation method and the cells for the CNT and PA (left) and plain PA (right) membranes. The free energy of the H_2O molecules and the Na^+ and Cl^- ions across the membrane are analyzed, and the results are plotted for (b) the nanocomposite CNT and PA membrane and (c) the plain PA membrane. The scarcity of ions in the center and bottom part of the membranes prevents the free-energy analysis in these areas. Trajectories for the water molecules across (d) the nanocomposite CNT and PA membrane and (e) the plain PA membrane. The different colors are used to represent different stages of the trajectory to facilitate its analysis.

where k_B is the Boltzmann constant, T is the temperature, (z) is the Z-density profile, and ρ is the average density of the Na^+, Cl^-, or water molecules (i). The analysis is performed within the membrane boundaries because the statistical information in the pure bulk water side is not suitable for free-energy discussion due to the resulting unrealistic very large values.

Figures 5(b) and 5(c) show the free energy (ΔG) of the ions and water molecules across the CNT and PA and plain PA membranes, respectively. Immediately after entering the membrane surface, the free energy of the water molecules rises to about 1.0 kcal/mol. These values at the interface near the membrane surface are in agreement with Ref. [56]. Because of the large solvated shell, the Na^+ and Cl^- ions require more energy when compared to water molecules to enter the membrane. Indeed, positively charged PA in our model has total net charge of $+3.18\ e$ and, consequently, can reject the positively charged sodium ions. Since our method to synthesize the CNT and PA membranes ensures that CNTs are embedded within the membrane, we expect this positive layer of PA to exert a strong electrostatic repulsion. However, Fig. 5(c) shows that due to their low solvation shell, the Na^+ show lower-free-energy values than the Cl^- due to their smaller hydration radius combined with the smaller VDW parameter results in lower short-range repulsion forces with the membrane atoms [57]; therefore, the effect of the solvation shells is more important than the plain electrostatic repulsion. It is important to note that the free energies of both ions in the proximity of the nanotube ($4.0 > z > 3.5$) [Fig. 5(b)] are lower than those compared at the same membrane depth in the plain PA [Fig. 5(c)]. This means that both ion permeations are thermodynamically favored; however, they are not definitive indicators of a higher salt permeation because this calculation does not consider water flow across the membrane. Indeed, the CNT and PA membrane also shows that water molecules have a lower free energy (average 0.79 kcal/mol) than plain PA (0.94 kcal/mol) for permeability, which indicates that water permeation is favored due to the CNT addition to the PA.

D. Water diffusion mechanism

One of the greatest potentials of MD is the better understanding of the water flow within reverse osmosis membranes [44,51]. In this context, we analyze several trajectories of water molecules to compare the water diffusion in the CNT and PA and the plain PA membranes. While in both cases the diffusion occurs by a clear hopping mechanism, the trajectories in the CNT and PA membrane have a more straightforward shape [Fig. 5(d)], while typical plain PA trajectories usually move back and forth several times until they cross the membrane [Fig. 5(e)]. A possible explanation for this phenomenon is that CNT creates a more hydrophilic region near the CNT surface because of the amide bond polarization resulting from the charge transfer between CNT and PA, thus, decreasing the free energy of water in that region and attracting water molecules in a shorter path where they can find this minimum. In order to leave this area, the molecules need again to enter a higher-free-energy section of the membrane; however, the short distance again allows the molecule to quickly find the other side of the membrane. This mechanism can be extended to a thick membrane if we consider the many carbon nanotubes surrounding the regions as low-free-energy wells that work like "rocks across a stream" which the water molecule can cross the membrane, following an oriented diffusion mechanism. In contrast, the homogeneity of the free-energy field in the PA membrane does not provide a clear minimum energy path, and, therefore, the trajectory is convoluted. This model requires a certain volume fraction of well-dispersed CNTs for the creation of a percolation path to effectively reduce the diffusion of water across the membrane. Indeed, we find experimentally that only nanotube concentrations close to 15 wt % can improve water permeation in the membranes. Higher CNT concentrations result in lower permeation membranes, which is understandable because the permeation path increases considerably due to the impermeability of CNTs, as discussed in a previous publication [24].

So far, we are aware only of theoretical models of combined percolation-diffusion in the literature [58], but to the best of our knowledge, there is no molecular dynamics study in which such diffusion has been described for a real system. A probable reason is that such a percolation-diffusion model requires a very large cell for atomistic MD, so we carry out a kinetic Monte Carlo simulation to explore this mechanism of diffusion, and the results are shown in Fig. 6. In the enlarged area in Fig. 6(b), we can see how the water molecule is moving using the low-free-energy areas of the sequentially labeled nanotubes to direct its path. When hopping from CNT to CNT, indeed, the trajectory seems to be less convoluted than a typical trajectory in a plain PA membrane shown for comparison in the enlarged area of Fig. 6(a). By simulating different CNT fractions, keeping the free energy of the matrix fixed, we find that the average permeation time decreases from 84 ns for the plain PA to 63 ns with 17 wt % of CNTs [Fig. 6(c)]. As expected, higher fractions of CNTs impose tortuosity paths and increase the permeation time to 66 ns at 20 wt %. It is seen that fractions of CNTs larger than 17% introduce a penalty to the diffusion path by imposing excessive tortuosity to the trajectories. Because of the simplicity and lower dimensionality of the simulation cell, we cannot translate these results to water flow, but it can provide a glimpse of the possible diffusion mechanism of the CNT and PA nanocomposite membranes. In these simulations, the low-free-energy areas are limited to only 2 nm from the CNT surface, which is the value resulting from molecular-dynamics calculations. However, we also have some experimental evidence from HRTEM observations of

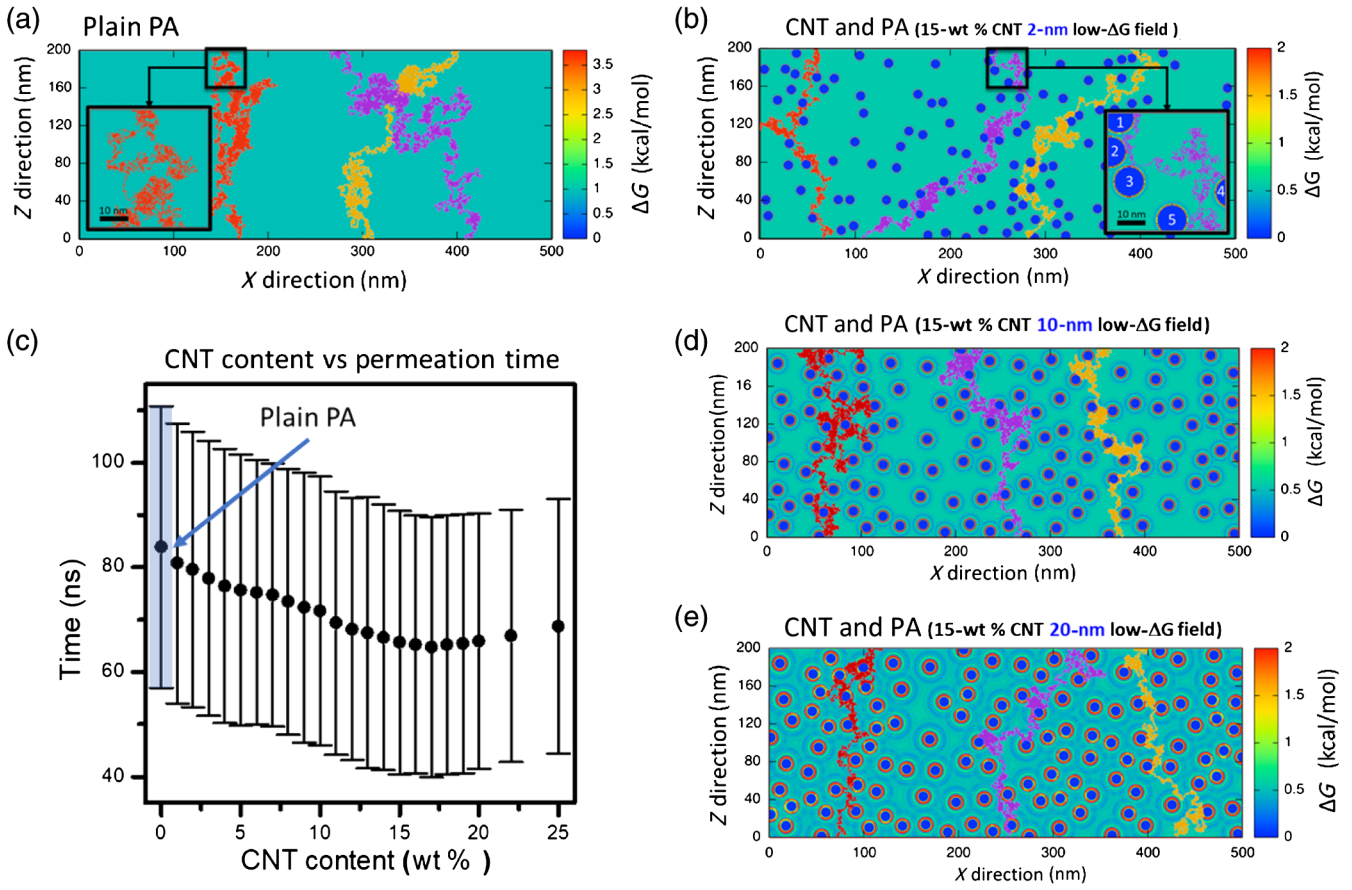

FIG. 6. Trajectories obtained by Monte Carlo simulation of water diffusion across 200-nm-thick reverse osmosis membranes. Trajectories are drawn using red, purple, yellow, and black lines to facilitate their visualization. (a) Plain PA membrane, (b) nanocomposite CNT and PA membrane with 15 wt % of CNTs and a low-free-energy field of 2 nm from the surface. CNT regions are forbidden areas and represented by blue circles. (c) Average values of permeation time as a function of CNT wt %. Additional results show the simulations for nanocomposite membranes containing 15 wt % of CNT with a low-free-energy structure that extends (d) 10 nm from the CNT surface and (e) 20 nm from the CNT surface. Increasing the low-free-energy area results in less convoluted trajectories.

12-nm-diameter CNTs that show in this case that an adsorbed PA layer can extend to at least 5–8 nm [13,24]. Thus, we carry out simulations extending proportionally the low-free-energy areas to 10 and 20 nm and the permeation time of the sample with 15 wt % decreases from 65 ns to 48 and 32 ns, respectively, due to straighter trajectories. These trajectories are shown in Figs. 6(d) and 6(e). However, additional experiments should be carried out in order to understand the PA microstructure in detail around the CNT and PA nanotubes.

IV. CONCLUSIONS

In this work, a study of the water diffusion mechanism across the nanocomposite CNT and PA reverse osmosis membranes is carried using a more detailed model that considers charge-transfer effects between the CNT and the PA. We find that CNTs create hydrophilic regions within the membrane that might direct the transport of water across the membrane by providing a lower-energy path. In this work, we use a charge equilibration method to improve the accuracy of the MD and propose a percolation-hopping mechanism for reverse osmosis composite membranes. We believe the correct understanding of the water diffusion mechanism will be useful for designing the optimal structure to improve the desalination performance of these promising types of reverse osmosis membranes.

ACKNOWLEDGMENTS

M. E., R. C. S., K. T., and T. H. are partly supported by the Japanese Society for the Promotion of Science Kakenhi Grant No. JP17H03401. We like to thank the Earth Simulator Center at the Japan Marine Science and Technology Center and Kyushu University for providing computational resources.

[1] J. R. Werber, A. Deshmukh, and M. Elimelech, The critical need for increased selectivity, not increased water permeability, for desalination membranes, Environ. Sci. Technol. Lett. 3, 112 (2016).

[2] K. P. Lee, T. C. Arnot, and D. Mattia, A review of reverse osmosis membrane materials for desalination—Development to date and future potential, J. Membr. Sci. **370**, 1 (2011).

[3] M. Fathizadeh, A. Aroujalian, and A. Raisi, Effect of added NaX nano-zeolite into polyamide as a top thin layer of membrane on water flux and salt rejection in a reverse osmosis process, J. Membr. Sci. **375**, 88 (2011).

[4] N. Ma, J. Wei, R. H. Liao, and C. Y. Y. Tang, Zeolite-polyamide thin film nanocomposite membranes: Towards enhanced performance for forward osmosis, J. Membr. Sci. **405**, 149 (2012).

[5] M. Safarpour, A. Khataee, and V. Vatanpour, Thin film nanocomposite reverse osmosis membrane modified by reduced graphene oxide/TiO_2 with improved desalination performance, J. Membr. Sci. **489**, 43 (2015).

[6] H. S. Lee, S. J. Im, J. H. Kim, H. J. Kim, J. P. Kim, and B. R. Min, Polyamide thin-film nanofiltration membranes containing TiO_2 nanoparticles, Desalination **219**, 48 (2008).

[7] J. T. Duan, E. Litwiller, and I. Pinnau, Preparation and water desalination properties of POSS-polyamide nanocomposite reverse osmosis membranes, J. Membr. Sci. **473**, 157 (2015).

[8] H. J. Kim, M. Y. Lim, K. H. Jung, D. G. Kim, and J. C. Lee, High-performance reverse osmosis nanocomposite membranes containing the mixture of carbon nanotubes and graphene oxides, J. Mater. Chem. A **3**, 6798 (2015).

[9] S. Bano, A. Mahmood, S. J. Kim, and K. H. Lee, Graphene oxide modified polyamide nanofiltration membrane with improved flux and antifouling properties, J. Mater. Chem. A **3**, 2065 (2015).

[10] F. Perreault, M. E. Tousley, and M. Elimelech, Thin-film composite polyamide membranes functionalized with biocidal graphene oxide nanosheets, Environ. Sci. Technol. Lett. **1**, 71 (2014).

[11] W. F. Chan, H. Y. Chen, A. Surapathi, M. G. Taylor, X. H. Hao, E. Marand, and J. K. Johnson, Zwitterion functionalized carbon nanotube/polyamide nanocomposite membranes for water desalination, ACS Nano **7**, 5308 (2013).

[12] H. Y. Zhao, S. Qiu, L. G. Wu, L. Zhang, H. L. Chen, and C. J. Gao, Improving the performance of polyamide reverse osmosis membrane by incorporation of modified multi-walled carbon nanotubes, J. Membr. Sci. **450**, 249 (2014).

[13] S. Inukai, R. Cruz-Silva, J. Ortiz-Medina, A. Morelos-Gomez, K. Takeuchi, T. Hayashi, A. Tanioka, T. Araki, S. Tejima, T. Noguchi, M. Terrones, and M. Endo, High-performance multi-functional reverse osmosis membranes obtained by carbon nanotube·polyamide nanocomposite, Sci. Rep. **5**, 13562 (2015).

[14] H. J. Kim, K. Choi, Y. Baek, D. G. Kim, J. Shim, J. Yoon, and J. C. Lee, High-performance reverse osmosis CNT/polyamide nanocomposite membrane by controlled interfacial interactions, ACS Appl. Mater. Interfaces **6**, 2819 (2014).

[15] J. N. Shen, C. C. Yu, H. M. Ruan, C. J. Gao, and B. Van der Bruggen, Preparation and characterization of thin-film nanocomposite membranes embedded with poly(methyl methacrylate) hydrophobic modified multiwalled carbon nanotubes by interfacial polymerization, J. Membr. Sci. **442**, 18 (2013).

[16] L. Zhang, G. Z. Shi, S. Qiu, L. H. Cheng, and H. L. Chen, Preparation of high-flux thin film nanocomposite reverse osmosis membranes by incorporating functionalized multi-walled carbon nanotubes, Desalin. Water Treat. **34**, 19 (2011).

[17] M. L. Lind, A. K. Ghosh, A. Jawor, X. F. Huang, W. Hou, Y. Yang, and E. M. V. Hoek, Influence of zeolite crystal size on zeolite-polyamide thin film nanocomposite membranes, Langmuir **25**, 10139 (2009).

[18] R. Cruz-Silva, M. Endo, and M. Terrones, Graphene oxide films, fibers, and membranes, Nano Rev. **5**, 377 (2016).

[19] K. Goh, H. E. Karahan, L. Wei, T. H. Bae, A. G. Fane, R. Wang, and Y. Chen, Carbon nanomaterials for advancing separation membranes: A strategic perspective, Carbon **109**, 694 (2016).

[20] M. Endo, Grow carbon fibers in the vapor phase, CHEMTECH, http://www.kroto.info/wp-content/uploads/2015/10/2.Chemtech1988.pdf.

[21] M. Endo, M. S. Strano, and P. M. Ajayan, Potential applications of carbon nanotubes, in *Carbon Nanotubes. Topics in Applied Physics*, edited by A. Jorio, G. Dresselhaus, and M. S. Dresselhaus (Springer, Berlin, Heidelberg, 2007), Vol. 111.

[22] M. Endo, T. Hayashi, Y. A. Kim, M. Terrones, and M. S. Dresselhaus, Applications of carbon nanotubes in the twenty-first century, Phil. Trans. R. Soc. A **362**, 2223 (2004).

[23] M. S. Dresselhaus, G. Dresselhaus, and R. Saito, Physics of carbon nanotubes, Carbon **33**, 883 (1995).

[24] T. Araki, R. Cruz-Silva, S. Tejima, K. Takeuchi, T. Hayashi, S. Inukai, T. Noguchi, A. Tanioka, T. Kawaguchi, M. Terrones, and M. Endo, Molecular dynamics study of carbon nanotubes/polyamide reverse osmosis membranes: Polymerization, structure, and hydration, ACS Appl. Mater. Interfaces **7**, 24566 (2015).

[25] J. Xu, Z. Wang, L. L. Yu, J. X. Wang, and S. C. Wang, A novel reverse osmosis membrane with regenerable anti-biofouling and chlorine resistant properties, J. Membr. Sci. **435**, 80 (2013).

[26] A. Tiraferri, C. D. Vecitis, and M. Elimelech, Covalent binding of single-walled carbon nanotubes to polyamide membranes for antimicrobial surface properties, ACS Appl. Mater. Interfaces **3**, 2869 (2011).

[27] H. D. Lee, H. W. Kim, Y. H. Cho, and H. B. Park, Experimental evidence of rapid water transport through carbon nanotubes embedded in polymeric desalination membranes, Small **10**, 2653 (2014).

[28] B. H. Jeong, E. M. V. Hoek, Y. S. Yan, A. Subramani, X. F. Huang, G. Hurwitz, A. K. Ghosh, and A. Jawor, Interfacial polymerization of thin film nanocomposites: A new concept for reverse osmosis membranes, J. Membr. Sci. **294**, 1 (2007).

[29] M. Amini, M. Jahanshahi, and A. Rahimpour, Synthesis of novel thin film nanocomposite (TFN) forward osmosis membranes using functionalized multi-walled carbon nanotubes, J. Membr. Sci. **435**, 233 (2013).

[30] J. K. Holt, H. G. Park, Y. M. Wang, M. Stadermann, A. B. Artyukhin, C. P. Grigoropoulos, A. Noy, and O. Bakajin, Fast mass transport through sub-2-nanometer carbon nanotubes, Science **312**, 1034 (2006).

[31] S. Plimpton, Fast parallel algorithms for short-range molecular-dynamics, J. Comput. Phys. **117**, 1 (1995).
[32] H. J. C. Berendsen, J. R. Grigera, and T. P. Straatsma, The missing term in effective pair potentials, J. Phys. Chem. **91**, 6269 (1987).
[33] W. D. Cornell, P. Cieplak, C. I. Bayly, I. R. Gould, K. M. Merz, D. M. Ferguson, D. C. Spellmeyer, T. Fox, J. W. Caldwell, and P. A. Kollman, A 2nd generation force-field for the simulation of proteins, nucleic-acids, and organic-molecules, J. Am. Chem. Soc. **117**, 5179 (1995).
[34] E. Harder, D. E. Walters, Y. D. Bodnar, R. S. Faibish, and B. Roux, Molecular dynamics study of a polymeric reverse osmosis membrane, J. Phys. Chem. B **113**, 10177 (2009).
[35] M. X. Ding, A. Szymczyk, and A. Ghoufi, On the structure and rejection of ions by a polyamide membrane in pressure-driven molecular dynamics simulations, Desalination **368**, 76 (2015).
[36] M. Shen, S. Keten, and R. M. Lueptow, Dynamics of water and solute transport in polymeric reverse osmosis membranes via molecular dynamics simulations, J. Membr. Sci. **506**, 95 (2016).
[37] J. M. Wang, W. Wang, P. A. Kollman, and D. A. Case, Automatic atom type and bond type perception in molecular mechanical calculations, J. Mol. Graphics Modell. **25**, 247 (2006).
[38] A. Jakalian, D. B. Jack, and C. I. Bayly, Fast, efficient generation of high-quality atomic charges. AM1-BCC model: II. Parameterization and validation, J. Comput. Chem. **23**, 1623 (2002).
[39] E. L. Pollock and J. Glosli, Comments on P(3)M, FMM, and the Ewald method for large periodic Coulombic systems, Comput. Phys. Commun. **95**, 93 (1996).
[40] A. K. Rappe and W. A. Goddard, Charge equilibration for molecular-dynamics simulations, J. Phys. Chem. **95**, 3358 (1991).
[41] H. M. Aktulga, J. C. Fogarty, S. A. Pandit, and A. Y. Grama, Parallel reactive molecular dynamics: Numerical methods and algorithmic techniques, Parallel Comput. **38**, 245 (2012).
[42] P. Giannozzi *et al.*, QUANTUM ESPRESSO: A modular and open-source software project for quantum simulations of materials, J. Phys. Condens. Matter **21**, 395502 (2009).
[43] J. P. Perdew, K. Burke, and M. Ernzerhof, Generalized Gradient Approximation Made Simple, Phys. Rev. Lett. **77**, 3865 (1996).
[44] V. Kolev and V. Freger, Hydration, porosity and water dynamics in the polyamide layer of reverse osmosis membranes: A molecular dynamics study, Polymer **55**, 1420 (2014).
[45] G. L. Vignoles, A hybrid random walk method for the simulation of coupled conduction and linearized radiation transfer at local scale in porous media with opaque solid phases, Int. J. Heat Mass Transfer **93**, 707 (2016).
[46] C. P. Calderon, L. Janosi, and I. Kosztin, Using stochastic models calibrated from nanosecond nonequilibrium simulations to approximate mesoscale information, J. Chem. Phys. **130**, 144908 (2009).
[47] G. Arya, H. C. Chang, and E. J. Maginn, A critical comparison of equilibrium, nonequilibrium and boundary-driven molecular dynamics techniques for studying transport in microporous materials, J. Chem. Phys. **115**, 8112 (2001).
[48] See the Supplemental Material at http://link.aps.org/supplemental/10.1103/PhysRevApplied.9.024018 for algorithm of the Kinetic Monte Carlo method, the parameters of free-energy and velocity of water derived from molecular dynamics, and the comparison of the charge transfer between an oligoamide and a graphene sheet by using first principles and QEq methods.
[49] O. Coronell, B. J. Marinas, and D. G. Cahill, Depth heterogeneity of fully aromatic polyamide active layers in reverse osmosis and nanofiltration membranes, Environ. Sci. Technol. **45**, 4513 (2011).
[50] V. Le Guilloux, P. Schmidtke, and P. Tuffery, FPOCKET: An open source platform for ligand pocket detection, BMC Bioinf. **10**, 168 (2009).
[51] M. J. Kotelyanskii, N. J. Wagner, and M. E. Paulaitis, Molecular dynamics simulation study of the mechanisms of water diffusion in a hydrated, amorphous polyamide, Comput. Theor. Polym. Sci. **9**, 301 (1999).
[52] M. X. Ding, A. Szymczyk, F. Goujon, A. Soldera, and A. Ghoufi, Structure and dynamics of water confined in a polyamide reverse-osmosis membrane: A molecular-simulation study, J. Membr. Sci. **458**, 236 (2014).
[53] H. Yan, X. P. Miao, J. Xu, G. Y. Pan, Y. Zhang, Y. T. Shi, M. Guo, and Y. Q. Liu, The porous structure of the fully-aromatic polyamide film in reverse osmosis membranes, J. Membr. Sci. **475**, 504 (2015).
[54] T. Wei, L. Zhang, H. Y. Zhao, H. Ma, M. S. J. Sajib, H. Jiang, and S. Murad, Aromatic polyamide reverse-osmosis membrane: An atomistic molecular dynamics simulation, J. Phys. Chem. B **120**, 10311 (2016).
[55] V. Kolev and V. Freger, Molecular dynamics investigation of ion sorption and permeation in desalination membranes, J. Phys. Chem. B **119**, 14168 (2015).
[56] Y. Luo, E. Harder, R. S. Faibish, and B. Roux, Computer simulations of water flux and salt permeability of the reverse osmosis FT-30 aromatic polyamide membrane, J. Membr. Sci. **384**, 1 (2011).
[57] D. E. Smith and L. X. Dang, Computer simulations of NaCl association in polarizable water, J. Chem. Phys. **100**, 3757 (1994).
[58] M. Barma and D. Dhar, Directed diffusion in a percolation network, J. Phys. C **16**, 1451 (1983).